Published in "Physical Review B 88(7): 075135, 2013"
which should be cited to refer to this work.

Nonequilibrium dynamical mean-field simulation of inhomogeneous systems

Martin Eckstein[1] and Philipp Werner[2]
[1]*Max Planck Research Department for Structural Dynamics, University of Hamburg-CFEL, Hamburg, Germany*
[2]*Department of Physics, University of Fribourg, 1700 Fribourg, Switzerland*

We extend the nonequilibrium dynamical mean field (DMFT) formalism to inhomogeneous systems by adapting the "real-space" DMFT method to Keldysh Green's functions. Solving the coupled impurity problems using strong-coupling perturbation theory, we apply the formalism to homogeneous and inhomogeneous layered systems with strong local interactions and up to 39 layers. We study the diffusion of doublons and holes created by photoexcitation in a Mott insulating system, the time-dependent build-up of the polarization and the current induced by a linear voltage bias across a multilayer structure, and the photoinduced current in a Mott insulator under bias.

I. INTRODUCTION

The study of nonequilibrium phenomena in correlated lattice systems has become an active research field due to experimental progress on several fronts. In cold atom systems, the interaction and bandwidth can be controlled via Feshbach resonances and the depth of the lattice potential, respectively, while the effect of external fields can be mimicked by shaking or tilting the optical lattice.[1–5] This allows us to investigate quench dynamics or field-driven effects in systems which may be viewed as ideal realizations of the simple model Hamiltonians typically considered in theoretical studies. On the other hand, advances in ultrafast laser science have made it possible to perturb a correlated material with a strong pulse and track the time evolution of the system with the (femtosecond) time resolution needed to observe intrinsically electronic processes.[6,7] Such experiments can provide new insights into the nature of correlated states of matter and may even lead to the discovery of "hidden phases," i.e., long-lived transient states that cannot be accessed via a thermal pathway.

Stimulated by these developments, a growing theoretical effort is aimed at describing and understanding the nonequilibrium properties of correlated lattice systems. Given the complexity of the task, much of this work has focused on the simplest relevant model, the one-band Hubbard model, which describes electrons that can hop between nearest-neighbor sites of some lattice with hopping amplitude t, and interact on-site with a repulsion energy U. A method which is well suited to capture strong local correlation effects is dynamical mean-field theory (DMFT),[8,9] and this formalism can be extended to nonequilibrium systems in a rather straightforward manner.[10,11] Over the last few years, nonequilibrium DMFT has been used in a large number of theoretical studies of the nonequilibrium dynamics in homogeneous bulk systems, including interaction quenches,[12,13] dc-field driven dynamics[11,14,15] or insulator-to-metal transitions[16,17] (and the related phenomenon of dimensional reduction[18]), photodoping,[19] ac-field induced band flipping,[20] and nonequilibrium phase transitions from antiferromagnetic to paramagnetic states.[21,22] While connecting these results to actual experiments is difficult because of the idealized setup in the model calculations, they have provided important insights into the relaxation dynamics of purely electronic systems, and the associated time scales and trapping phenomena.

One step towards more realistic model calculations is to switch from infinitely extended, homogenous systems to a description which allows for a spatial variation in the model parameters. In equilibrium, the "real-space" or "inhomogeneous" DMFT approach[23,24] allows us, for example, to describe some effect of the trapping potential in cold-atom experiments,[25,26] or correlation effects in artificially designed heterostructures.[23,24,27,28] In a direct generalization of this real-space DMFT to nonequilibrium, one would have to store and manipulate Green's functions $G_{ij}(t,t')$ which depend on two space arguments i,j and on two time arguments. Decoupling of space and time is no longer possible, neither by introducing momentum-dependent Green's functions $G_{\boldsymbol{k}}(t,t')$ (as in homogeneous nonequilibrium DMFT), nor by using frequency-dependent Green's functions $G_{ij}(\omega)$ (as in inhomogeneous equilibrium DMFT). The fully inhomogeneous setup would thus require a prohibitively large amount of memory for most applications. However, the problem turns out to be numerically tractable for a simpler layered geometry, which is still relevant for many applications. Here one considers a system in which the properties can change as a function of the lattice position in one direction, while being homogeneous in the $d-1$ other dimensions. For example, such an extension allows us to deal with surface phenomena in condensed matter systems, such as the propagation of excitations from the surface of a sample into the bulk (which has been looked at recently within a time-dependent Gutzwiller approach[29]). In this context it is important to mention that pump-probe experiments often excite only a thin surface layer, such that interesting phenomena must be inferred by subtracting the bulk signal, based on some assumptions about the penetration depth of the pump pulse. The layer description also naturally lends itself to the study of interfaces and heterostructures.[30–32] The latter are at present the subject of extensive research, and experimental results on ultrafast photoinduced metal-insulator transitions in heterostructures have recently been published.[33]

In this paper we discuss and test an implementation of the nonequilibrium DMFT formalism for inhomogeneous, layered structures. This formalism is an adaptation of the equilibrium "real-space" or "inhomogeneous" DMFT method developed by Potthoff, Nolting, Freericks, and others.[23,24] We discuss the formalism and the techniques used for solving the DMFT equations in Sec. II, and illustrate the versatility of the approach

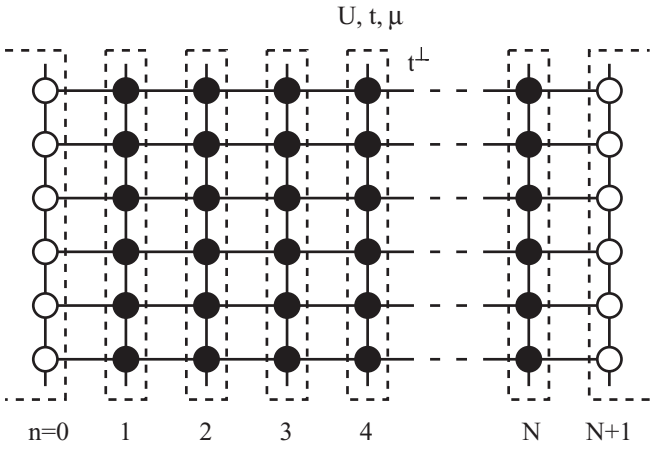

FIG. 1. Illustration of the layer setup with N correlated layers (full dots), intralayer hopping t, interlayer hopping $t^\perp$, interaction U, and chemical potential μ (all these parameters can be layer and time dependent). The boundary condition is given either by coupling to some noninteracting equilibrium bath, by a vacuum (no hopping into the boundary layers), or by repeating the hybridization functions of the surface layers.

in Sec. III with several test calculations involving electric field pulse excitations of correlated layers or heterostructures. Section IV gives a brief conclusion and outlook.

II. MODEL AND METHOD

The approximate DMFT treatment of layered structures assumes a local self-energy for each layer and maps the system to an effectively one-dimensional model subject to a self-consistency condition. An efficient strategy for solving the DMFT equations, which involves a partial Fourier transformation of the Green's functions with respect to the transverse space directions, has been proposed by Potthoff and Nolting,[23] and a detailed description of the equilibrium implementation of this so-called "inhomogeneous DMFT" can be found in work by Freericks.[24,34] Here we extend this technique to nonequilibrium systems in order to describe pulse excitations of surfaces or heterostructures, as well as transport through correlated thin films, using the nonequilibrium DMFT formalism.[10,11]

We consider a Hubbard model with N layers, connected by an interlayer hopping $t^\perp$, and either "vacuum," "lead," or "bulk" boundary conditions applied to the left ($n = 1$) and right ($n = N$) surface layers (see Fig. 1). Here "vacuum" means no hopping to the boundary layer, "lead" means we impose some equilibrium DMFT solution in the boundary layer, and "bulk" means that the solution on the surface layer is repeated periodically. The corresponding Hamiltonian is given by

$$\begin{aligned} H = &\sum_{n=1}^{N}\Bigg[-\sum_{ij\sigma} t^{\parallel}_{n,ij}\, c^\dagger_{i,n,\sigma} c_{j,n,\sigma} + \epsilon_{\mathrm{loc},n}\sum_{i\sigma} c^\dagger_{i,n,\sigma} c_{i,n,\sigma}\Bigg] \\ &+ \sum_{n=1}^{N}\sum_{i} U_n\, c^\dagger_{i,n,\uparrow} c_{i,n,\uparrow} c^\dagger_{i,n,\downarrow} c_{i,n,\downarrow} \\ &+ \sum_{n=1}^{N-1}\sum_{i\sigma}(-t^\perp_n c^\dagger_{i,n,\sigma} c_{i,n+1,\sigma} + \mathrm{H.c.}) + \text{ b.t.}, \end{aligned} \tag{1}$$

where $c^\dagger_{i,n,\sigma}$ creates an electron on lattice site i in layer n, U_n is the on-site Coulomb interaction in layer n, $\epsilon_{\mathrm{loc},n}$ is a layer-dependent on-site potential, and $t^\parallel$ and $t^\perp$ denote the hopping within the layers and between the layers, respectively. The term "b.t." stands for the boundary terms as described above. All parameters can depend both on time and on the layer index, which will mostly not be shown explicitly in the following. In the actual implementation, each layer corresponds to a d-dimensional hypercubic lattice with lattice spacing a, and we present results for $d = 1$. This does not mean that we intend to study specific properties of a two-dimensional (2D) Hubbard model. The DMFT approximation always yields the generic behavior of a high-dimensional layer, even if a one-dimensional (1D) density of states is used within the self-consistency loop. The advantage of the 1D layer is that calculations in the presence of a time-dependent electric field become substantially cheaper than in $d > 1$, because an explicit integral over the Brillouin zone must be performed (see below). We will later switch to the Fourier transformation with respect to the intralayer coordinate $c_{j,n,\sigma} = \frac{1}{\sqrt{N_k}}\sum_{\boldsymbol{k}} e^{i\boldsymbol{k}\boldsymbol{r}_j/a} c_{\boldsymbol{k},n,\sigma}$. The intralayer hopping Hamiltonian becomes $\sum_{\boldsymbol{k}\sigma}\epsilon_{n,\boldsymbol{k}}\, c^\dagger_{\boldsymbol{k},n,\sigma} c_{\boldsymbol{k},n,\sigma}$, with the dispersion $\epsilon_{n,\boldsymbol{k}} = -\sum_i t^{\parallel}_{n,ij} e^{i\boldsymbol{k}(\boldsymbol{r}_j-\boldsymbol{r}_i)/a}$.

External electromagnetic fields are included in Eq. (1) via the Peierls substitution: We consider electric fields $\boldsymbol{E} \equiv (\boldsymbol{E}^\parallel_n, E^\perp_n)$ that depend only on the layer coordinate, and let $\boldsymbol{E}^\parallel_n$ and $E^\perp_n$ denote the parallel field component in layer n and the perpendicular field component between layer n and $n+1$, respectively. Units for the fields are taken as $[t]/ea$ for $\boldsymbol{E}^\parallel$ and $[t]/ea_\perp$ for $E^\perp$, where $[t]$ is the unit of energy, $a_\perp$ is the spacing between layers, and $-e$ is the electron charge. In a gauge where also the scalar potential ϕ_n and vector potential $\boldsymbol{A} \equiv (\boldsymbol{A}^\parallel_n, A^\perp_n)$ depend on the layer only, we then have $\boldsymbol{E}^\parallel_n = -\partial_t \boldsymbol{A}^\parallel_n$ and $\boldsymbol{E}^\perp_n = -\partial_t A^\perp_n - (\phi_{n+1} - \phi_n)$, and the Peierls substitution gives

$$\epsilon_{n,\boldsymbol{k}} = \tilde{\epsilon}_{n,\boldsymbol{k}+\boldsymbol{A}^\parallel_n}, \tag{2}$$

$$t^\perp_n = \tilde{t}^\perp_n \exp(iA^\perp_n), \tag{3}$$

$$\epsilon_{\mathrm{loc},n} = \tilde{\epsilon}_{\mathrm{loc},n} - \phi_n, \tag{4}$$

where quantities with a tilde correspond to zero field. Also for fields perpendicular to the layer, it is often convenient to use a gauge with zero scalar potential.

Nonequilibrium DMFT provides a set of equations for the space- and time-dependent Green's functions $G_{i,n;j,m}(t,t') = -i\langle \mathcal{T}_\mathcal{C} c_{i,n,\sigma}(t) c^\dagger_{j,m,\sigma}(t')\rangle$. Here t and t' lie on the L-shaped Kadanoff-Baym contour $\mathcal{C}$, and $\mathcal{T}_\mathcal{C}$ is the contour-ordering operator. The notation for contour-ordered Green's functions and their inverse operators, as well as for the contour δ function $\delta_\mathcal{C}(t,t')$ and integration $\int_\mathcal{C} dt$, is adopted from Ref. 13. The functions $G_{i,n;j,m}(t,t')$ are obtained from the lattice Dyson equation with a local but layer-dependent self-energy $\Sigma_n(t,t')$, which is computed from an effective impurity model (see below; for simplicity we omit a possible dependence of local quantities on spin). Due to the translational invariance within the layers, one can perform a Fourier transformation in the transverse directions and introduce

the momentum-dependent Green's functions $G_{\boldsymbol{k};n,m}(t,t') = -i\langle \mathcal{T}_{\mathcal{C}} c_{\boldsymbol{k},n,\sigma}(t) c^{\dagger}_{\boldsymbol{k},m,\sigma}(t')\rangle$. The Dyson equation then decouples for each $\boldsymbol{k}$, and one has the following matrix expression for the $N \times N$ matrices $(G_{\boldsymbol{k}})_{n,m} \equiv G_{\boldsymbol{k};n,m}$:

$$\begin{aligned}\left(G^{-1}_{\boldsymbol{k}}\right)_{m,n}(t,t') = \{&\delta_{\mathcal{C}}(t,t')[i\partial_t + \mu - \epsilon_{\mathrm{loc},m} - \epsilon_{\boldsymbol{k},m}(t)] \\ &- \Sigma_m(t,t')\}\delta_{m,n} - \delta_{\mathcal{C}}(t,t')\{t^{\perp}_m(t)\delta_{m+1,n} \\ &+ [t^{\perp}_{m-1}(t)]^*\delta_{m-1,n}\},\end{aligned} \tag{5}$$

which is equivalent to the Dyson equation for a one-dimensional chain with sites $m = 1,\ldots,N$. Note that the inverse Green's function in this equation is an integral-differential operator, and the Dyson equation for two-time Keldysh Green's functions $\int_{\mathcal{C}} d\bar{t}\, G^{-1}(t,\bar{t})G(\bar{t},t') = \delta_{\mathcal{C}}(t,t')$ is essentially equivalent to a set of integral-differential equations known as the Kadanoff-Baym equations.[35] Hence the matrix structure in Eq. (5) defines an $N \times N$ set of coupled integral-differential equations. The local Green's function on layer n is then computed from $G_n = \frac{1}{N_{\boldsymbol{k}}}\sum_{\boldsymbol{k}}(G_{\boldsymbol{k}})_{n,n}$, and hence we only need the diagonal elements $(G_{\boldsymbol{k}})_{n,n}$ of the momentum-dependent Green's function. These can be obtained by expressions which are analogous to the following formulas for the inverse of a tridiagonal matrix:

$$M^{-1} = \begin{pmatrix} z-a_1 & b_1 & & & \\ b_1^* & z-a_2 & b_2 & & \\ & & \cdots & & \\ & & & \cdots & b_{n-1} \\ & & & b^*_{n-1} & z-a_n \end{pmatrix}, \tag{6}$$

$$M_{11} = \frac{1}{z-a_1 - \frac{|b_1|^2}{z-a_2-\frac{|b_2|^2}{z-a_3-\cdots}}}, \tag{7}$$

$$M_{22} = \frac{1}{z-a_2 - \frac{|b_1|^2}{z-a_1} - \frac{|b_2|^2}{z-a_3-\frac{|b_3|^2}{z-a_4-\cdots}}}, \tag{8}$$

$$M_{33} = \frac{1}{z-a_3 - \frac{|b_2|^2}{z-a_2-\frac{|b_1|^2}{z-a_1}} - \frac{|b_3|^2}{z-a_4-\frac{|b_4|^2}{z-a_5-\cdots}}}, \tag{9}$$

$\ldots.$

Explicitly, taking into account the correct order of the time-dependent factors, one finds

$$(G_{\boldsymbol{k}})_{n,n} = \frac{1}{g^{-1}_{\boldsymbol{k},n} - \Delta^L_{\boldsymbol{k},n-1} - \Delta^R_{\boldsymbol{k},n+1}}, \tag{10}$$

$$g^{-1}_{\boldsymbol{k},n} = i\partial_t + \mu - \epsilon_{\mathrm{loc},n} - \epsilon_{\boldsymbol{k},n} - \Sigma_n, \tag{11}$$

where $g_{\boldsymbol{k},n}$ is the Green's function corresponding to an isolated layer, and we have introduced the products

$$\Delta^L_{\boldsymbol{k},n-1}(t,t') = t^{\perp *}_{n-1}(t)\, G^{[n]}_{\boldsymbol{k},n-1}(t,t')\, t^{\perp}_{n-1}(t') \tag{12}$$

$$\equiv t^{\perp *}_{n-1} * G^{[n]}_{\boldsymbol{k},n-1} * t^{\perp}_{n-1}, \tag{13}$$

$$\Delta^R_{\boldsymbol{k},n+1}(t,t') = t^{\perp}_{n}(t)\, G^{[n]}_{\boldsymbol{k},n+1}(t,t')\, t^{\perp *}_{n}(t'), \tag{14}$$

which involve the Green's functions $G^{[n]}_{\boldsymbol{k}}$ for the "chain" [Eq. (5)] with site n removed. The Green's functions $G^{[n]}_{\boldsymbol{k}}$ satisfy equations analogous to Eq. (10), such that we obtain for the hybridizations $\Delta^L_{\boldsymbol{k},n}$ and $\Delta^R_{\boldsymbol{k},n}$,

$$\Delta^L_{\boldsymbol{k},n} = t^{\perp *}_n * \frac{1}{g^{-1}_{\boldsymbol{k},n} - \Delta^L_{\boldsymbol{k},n-1}} * t^{\perp}_n, \tag{15}$$

$$\Delta^R_{\boldsymbol{k},n} = t^{\perp}_{n-1} * \frac{1}{g^{-1}_{\boldsymbol{k},n} - \Delta^R_{\boldsymbol{k},n+1}} * t^{\perp *}_{n-1}, \tag{16}$$

for layers $n = 1,\ldots,N$. The boundary conditions read $\Delta_{\boldsymbol{k},n} = 0$ (vacuum) or $\Delta_{\boldsymbol{k},n} = \Delta_{\boldsymbol{k},\mathrm{lead}}$ (lead) for $n = 0, N+1$. The bulk boundary condition is $\Delta^R_{N+1} = \Delta^R_N$, $\Delta^L_0 = \Delta^L_1$. Once the $\Delta^L_{\boldsymbol{k},n-1}$ and $\Delta^R_{\boldsymbol{k},n+1}$ for a given layer n have been updated, one computes $(G_{\boldsymbol{k}})_{n,n}$ using Eq. (10), and determines the hybridization function $\Lambda_n = \Lambda_n[G_n]$ of the impurity model by solving the impurity Dyson equation,

$$G_n = \frac{1}{N_{\boldsymbol{k}}}\sum_k (G_{\boldsymbol{k}})_{n,n} \equiv \frac{1}{i\partial_t + \mu - \epsilon_{\mathrm{loc},n} - \Sigma_n - \Lambda_n}. \tag{17}$$

The solution of the impurity problem [in the present case, we use the noncrossing approximation (NCA)[36,37] as impurity solver] yields an updated G_n and Σ_n.

A self-consistent solution on all layers can hence be obtained by the "zipper algorithm"[24]:

$$\begin{array}{lccccc} n=1 & \downarrow & & \uparrow & & \downarrow \\ n=2 & \downarrow & & \uparrow & & \downarrow \\ \ldots & \downarrow & \Delta^L_n & \uparrow & \Delta^R_n, G_n, \Lambda_n & \downarrow \quad \Delta^L_n, G_n, \Lambda_n \\ & \downarrow & & \uparrow & & \downarrow \\ n=N & \downarrow & & \uparrow & & \ldots, \end{array}$$

where we start for example with $\Lambda_n = \Lambda_{\mathrm{bulk}}$, $\Sigma_n = \Sigma_{\mathrm{bulk}}$, for $n = 1,\ldots,N$, $\Delta^L_1 = \Delta^R_N = 0$, and then update Δ^L_n using Eq. (15) from $n = 1$ to N. On the way back, we use Eq. (16) to update Δ^R_n, from $n = N$ to $n = 1$, and at the same time compute G_n, Λ_n, and Σ_n for each of these n, and so on.

Equations (10)–(17) are integral-differential equations on the contour $\mathcal{C}$. Following the strategy outlined in Ref. 19, we can cast these equations in a form that can conveniently be handled by numerically stable "time-stepping" procedures for the propagation of Green's functions in real time. Defining the variables $\xi_{\boldsymbol{k},n} = \epsilon_{\boldsymbol{k},n} + \Delta^L_{\boldsymbol{k},n-1} + \Delta^R_{\boldsymbol{k},n+1}$ and $Z_n = [i\partial_t + \mu - \epsilon_{\mathrm{loc},n} - \Sigma_n]^{-1}$, one can write Eqs. (10) and (17) in the form (dropping for simplicity the index n everywhere)

$$[Z^{-1} - \xi_{\boldsymbol{k}}] * G_{\boldsymbol{k}} = I, \quad I = G_{\boldsymbol{k}} * [Z^{-1} - \xi_{\boldsymbol{k}}], \tag{18}$$

$$[Z^{-1} - \Lambda] * G = I, \quad I = G * [Z^{-1} - \Lambda]. \tag{19}$$

By summing Eq. (18) over $\boldsymbol{k}$ and comparing with Eq. (19), one finds $G^{(1)} \equiv \sum_{\boldsymbol{k}} \xi_{\boldsymbol{k}} * G_{\boldsymbol{k}} = \Lambda * G$ and $G^{(1)^\dagger} \equiv \sum_{\boldsymbol{k}} G_{\boldsymbol{k}} * \xi_{\boldsymbol{k}} = G * \Lambda$. We next take the second of Eqs. (19) and multiply from the right with Z. This leads to

$$[I + G * \Lambda] * Z = [I + G^{(1)^\dagger}] * Z = G, \tag{20}$$

which we can solve for Z (after having evaluated $G^{(1)^\dagger} = G * \Lambda$). Multiplying the first of Eqs. (18) from the left with Z gives

$$[I - Z * \xi_{\boldsymbol{k}}] * G_{\boldsymbol{k}} = Z, \tag{21}$$

which we can solve for $G_{\boldsymbol{k}}$. From the first Eq. (19), we also get $[I + \Lambda * G] * \Lambda = Z^{-1} * G * \Lambda = \sum_{\boldsymbol{k}} Z^{-1} * G_{\boldsymbol{k}} *$

$\xi_{\boldsymbol{k}}$. But from the first Eq. (18), $Z^{-1} * G_{\boldsymbol{k}} = I + \xi_{\boldsymbol{k}} * G_{\boldsymbol{k}}$, so

$$[I + \Lambda * G] * \Lambda = [I + G^{(1)}] * \Lambda = G^{(2)}, \qquad (22)$$

where $G^{(2)} = \sum_{\boldsymbol{k}} (\xi_{\boldsymbol{k}} + \xi_{\boldsymbol{k}} * G_{\boldsymbol{k}} * \xi_{\boldsymbol{k}})$. The solution of Eq. (22) yields Λ.

To solve Eqs. (15) and (16), we first compute $g_{\boldsymbol{k},n}$ [Eq. (11)] by solving

$$[I - Z_n * \epsilon_{\boldsymbol{k}}] * g_{\boldsymbol{k},n} = Z_n. \qquad (23)$$

With the shorthand notation $\tilde{\Delta}^L_{\boldsymbol{k},n} = (G^{[n+1]}_{\boldsymbol{k}})_n$ and $\tilde{\Delta}^R_{\boldsymbol{k},n} = (G^{[n-1]}_{\boldsymbol{k}})_n$, we rewrite Eqs. (15) and (16) as

$$\left[I - g_{\boldsymbol{k},n} * t^{\perp *}_{n-1} * \tilde{\Delta}^L_{\boldsymbol{k},n-1} * t^{\perp}_{n-1}\right] * \tilde{\Delta}^L_{\boldsymbol{k},n} = g_{\boldsymbol{k},n}, \qquad (24)$$

$$\left[I - g_{\boldsymbol{k},n} * t^{\perp}_{n} * \tilde{\Delta}^R_{\boldsymbol{k},n+1} * t^{\perp *}_{n}\right] * \tilde{\Delta}^R_{\boldsymbol{k},n} = g_{\boldsymbol{k},n}. \qquad (25)$$

Equations (20)–(25) are all of the form $[I + A] * X = B$ and have to be solved for X. This is an integral equation of the Volterra type, which is well behaved and which we solve using the techniques described in Ref. 13. The solution can be obtained by successively increasing the maximum time in a step by step manner, thereby not modifying an already converged solution at earlier times.

In summary, at a given time step, we perform the following calculations in layer n:

1. For given Λ_n, solve impurity problem (NCA equations) to obtain G_n.
2. Evaluate $G^{(1)\dagger}_n = G_n * \Lambda_n$, solve Eq. (20) for Z_n.
3. For each $\boldsymbol{k}$ point,
   (a) solve Eq. (23) for $g_{\boldsymbol{k},n}$,
   (b) solve equations of the type (25) and (24) to get the new $\tilde{\Delta}^R_{\boldsymbol{k},n}$ or $\tilde{\Delta}^L_{\boldsymbol{k},n}$, and compute $\Delta^R_{\boldsymbol{k},n}$ or $\Delta^L_{\boldsymbol{k},n}$ from Eqs. (12) and (14) (depending on the direction of the sweep),
   (c) define $\xi_{\boldsymbol{k},n} = \epsilon_{\boldsymbol{k}} + \Delta^L_{\boldsymbol{k},n-1} + \Delta^R_{\boldsymbol{k},n+1}$ and solve Eq. (21) for $G_{\boldsymbol{k},n}$.
4. Having obtained $\xi_{\boldsymbol{k},n}$ and $G_{\boldsymbol{k},n}$ for all $\boldsymbol{k}$ points, calculate $G^{(1)}_n$ and $G^{(2)}_n$.
5. Solve Eq. (22) to obtain the new Λ_n.

Then we move to the next layer, where we repeat the same cycle, zipping back and forth until convergence is reached. Only a few cycles are needed for convergence, since a very good starting point is obtained by extrapolating the Green's functions from earlier times.

Depending on the application, it may be desirable to include a dissipation mechanism which allows us to remove energy injected into the system by a quench or external field. In Ref. 38 we have briefly described how one can locally couple a phonon bath with given temperature. Let us discuss now how such a bath can be incorporated into the "zipper algorithm." In our approximation, the electronic self-energy on layer n is the sum of an electronic contribution $\Sigma_U[G_n]$ and of a bath contribution $\Sigma_{\rm diss}[G_n]$. As in the case without bath [Eq. (17)], $\Sigma_U[G_n]$ is obtained from the solution of the impurity problem with hybridization Λ_n: $G_n = G_n[\Lambda_n]$, with

$$G_n = \frac{1}{i\partial_t + \mu - \Sigma_U[G_n] - \Lambda_n}. \qquad (26)$$

The bath contribution is approximated by the lowest order Holstein-type electron-phonon diagram:

$$\Sigma_{\rm diss}[G_n] = \lambda^2 G_n(t,t') D(t,t'), \qquad (27)$$

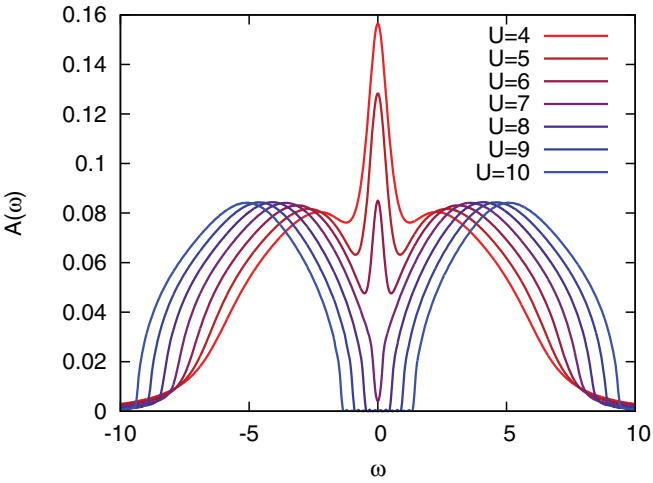

FIG. 2. (Color online) Equilibrium spectral functions for an infinite system of 1D layers, at $\beta = 5$ and indicated values of the interaction strength. The DMFT solution has been obtained with an NCA impurity solver, which yields reliable results in the insulating phase.

with $D(t,t') = -i\mathrm{Tr}[T_{\mathcal{C}} \exp(-i \int_{\mathcal{C}} dt\, \omega_0 b^\dagger b) b(t) b^\dagger(t')]/Z$ the equilibrium boson propagator for boson frequency ω_0 and coupling strength λ. Therefore, in Eqs. (10) and (11), which relate the momentum dependent lattice Green's function to the self-energy, we have to replace Σ_n by $\Sigma_U[G_n] + \Sigma_{\rm diss}[G_n]$, or equivalently $\epsilon_{\boldsymbol{k}}$ by $\epsilon_{\boldsymbol{k}} + \Sigma_{\rm diss}[G_n]$.[38]

In practice, we define $Z_{\rm latt} = [i\partial_t + \mu - \epsilon_{{\rm loc},n} - \Sigma_U - \Sigma_{\rm diss}]^{-1}$ (dropping the layer-index n), so that Eq. (26) becomes $G = 1/(Z^{-1}_{\rm latt} - \Lambda_{\rm latt})$, with $\Lambda_{\rm latt} = \Lambda - \Sigma_{\rm diss}$. We may then repeat the derivation of Eqs. (19)–(22) with the substitution $\Lambda \to \Lambda_{\rm latt}$, $Z \to Z_{\rm latt}$, i.e., given $\Lambda_{\rm latt}$ and G, $Z_{\rm latt}$ is computed from $[I + G^{(1)\dagger}] * Z_{\rm latt} = G$ (with $G^{(1)\dagger} = G * \Lambda_{\rm latt}$), then a new $\Lambda_{\rm latt}$ is obtained from the solution of $[I + G^{(1)}] * \Lambda_{\rm latt} = G^{(2)}$. Finally, $\Lambda = \Lambda_{\rm latt} + \Sigma_{\rm diss}$ is used as input for the impurity solver.

III. RESULTS

A. Test of the implementation

In this work we will consider one-dimensional layers, and use the intralayer hopping $t^{\parallel} = 1$ as the unit of energy. The equilibrium spectral function for an infinite system of such 1D layers and interlayer hopping $t^{\perp} = 1$ (corresponding to the DMFT solution of the 2D Hubbard model) is shown in Fig. 2, for inverse temperature $\beta = 5$ and indicated values of U. The impurity problem was solved with NCA on the Keldysh contour and the spectra were obtained via Fourier transformation of the retarded Green's function. Around $U = 7$, a Mott gap opens in a continuous fashion (crossover). Since we cannot reliably study the low temperature behavior of the metallic phase within NCA, we will not investigate this transition in further detail. In the following, we will mostly focus on the insulating regime ($U > 7$).

A good test of the implementation and its accuracy is the calculation of the total energy. The total energy, normalized by the number of sites in the transverse direction, has a local

contribution

$$E_{\rm pot} = \sum_{m=1}^{N} [U_m d_m + (\epsilon_{{\rm loc},m} - \mu) n_m], \tag{28}$$

where d_m is the double occupancy and $n_m = n_{m\uparrow} + n_{m\downarrow}$ is the occupation on layer m. In addition there is the intralayer kinetic energy

$$E_{\rm kin,intra} = \sum_{m=1}^{N} \sum_{k\sigma} \epsilon_{k,m} n_{k,m,\sigma}, \tag{29}$$

and the interlayer kinetic energy

$$E_{\rm kin,inter} = -\sum_{m=1}^{N-1} \sum_{k\sigma} t_m^{\perp} \langle c^{\dagger}_{k,m,\sigma} c_{k,m+1,\sigma} \rangle + {\rm H.\,c.}, \tag{30}$$

where we have assumed vacuum boundary conditions. To evaluate Eq. (30) we note that $t_m^{\perp} \langle c^{\dagger}_{k,m,\sigma} c_{k,m+1,\sigma} \rangle = -i t_m^{\perp} G^{<}_{k,m+1,m}(t,t)$ and $t_m^{\perp} G_{k,m+1,m} = \Delta^{R}_{k,m+1} * G_{k,m}$. The latter identity follows from a comparison of the Dyson equation (5) with Eq. (10).

If an electric field is applied to the system, a current j will be induced (j is defined as the particle current, not including the electric charge -1),

$$j_m^{\parallel} = \sum_{k\sigma} (\partial_k \epsilon_{k,m}) n_{k,m,\sigma}, \tag{31}$$

$$j_m^{\perp} = -i \sum_{k\sigma} t_m^{\perp} \langle c^{\dagger}_{k,m,\sigma} c_{k,m+1,\sigma} \rangle - {\rm H.c.}, \tag{32}$$

where $j_m^{\parallel}$ is the intralayer component, and $j_m^{\perp}$ is the current from layer m to $m+1$. While the electric field is applied, the total energy will change like $dE_{\rm tot}/dt = -\sum_m \boldsymbol{j}_m \boldsymbol{E}_m$ (for electrons with charge -1). Here we assume vacuum boundary conditions (and thus $j_0^{\perp} = j_N^{\perp} = 0$), because otherwise energy can flow from the system into the leads. A good check of the numerics is thus to verify that $E_{\rm tot}(t) - E_j(t)$ is time independent, where $E_j(t) = -\int_0^t d\bar{t} [\sum_{m=1}^{N} j_m^{\parallel}(\bar{t}) E_m^{\parallel}(\bar{t}) + \sum_{m=1}^{N-1} j_m^{\perp}(\bar{t}) E_m^{\perp}(\bar{t})]$ is the absorbed energy. After the pulse, the Hamiltonian of the system is time independent, and the total energy should thus also become time independent. In Fig. 3 we plot the time evolution of the different energy contributions for a nine-layer system consisting of three metallic layers ($U = 4$) sandwiched between Mott insulating layers ($U = 15$). The perturbation is an in-plane, few-cycle electric field pulse of frequency $\Omega \approx 12$ (see inset), which is applied to all nine layers. (For the time propagation, we use a time-step $\Delta t = 0.02$ in combination with a fifth order integration scheme, and we have verified that our results are not affected by the time discretization.)

This strong pulse creates doublon-hole pairs and leads to a rapid increase in the potential energy. After the pulse, one observes a redistribution of potential energy into kinetic energy in such a way that the total energy is conserved. Also, the change in total energy is equal to the absorbed energy E_j, so that $E_{\rm tot} - E_j$ remains zero within the numerical accuracy. That this result is a nontrivial check follows from the lower panels, which show the time evolution of the double occupancy and intralayer kinetic energy in all nine layers. These curves indicate that doublons and holes move from the insulating regions to the metallic region, where they recombine, heat up the metal, and lead to an increase in the intralayer kinetic energy.

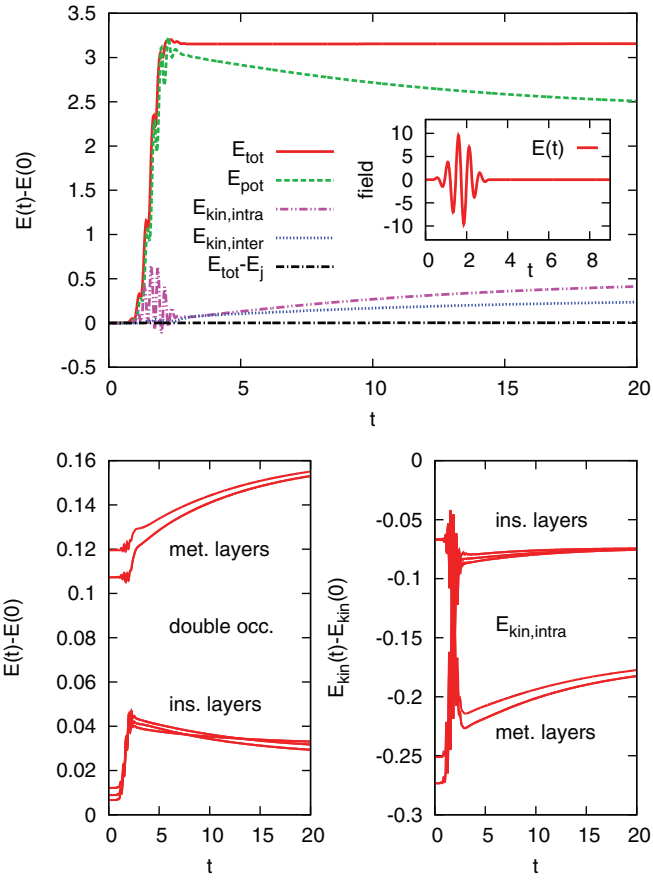

FIG. 3. (Color online) Test of the energy calculation for a heterostructure composed of nine 1D layers with $t^{\perp} = 1$, interaction $U = 15$ on layers 1, 2, 3, 7, 8, and 9 and $U = 4$ on layers 4, 5, and 6, with vacuum boundary conditions. The electric field pulse shown in the inset is applied to all the layers.

B. Doublon diffusion

As a first application we consider the spreading of photoexcited doublons and holes in a Mott insulator. The system consists of 39 layers and we employ the "repeated" boundary condition to minimize boundary effects. The doublons and holes are created in the central layer ($m = 20$) by the application of an in-plane electric field pulse with $\Omega \approx 12$, centered at $t_{\rm pulse} = 1.7$, which lasts up to $t = 3$. This setup may not be realistic from an experimental point of view, but it allows us to study how artificially created carriers spread out inside a Mott insulating bulk. On the time scale of the present simulation, we can ignore the recombination of doublons and holes. This is consistent with corresponding DMFT calculations for a homogeneously excited bulk system, which indicate that the lifetime of these carriers depends exponentially on the interaction U in the Mott insulating regime.[19] Note that we will always measure and plot the double occupancy $d(t) = \langle n_\uparrow(t) n_\downarrow(t) \rangle$, which already takes a small nonzero value in the initial state with no doublons, due to virtual charge excitations. Because the contribution of these quantum fluctuations is not changed to first order

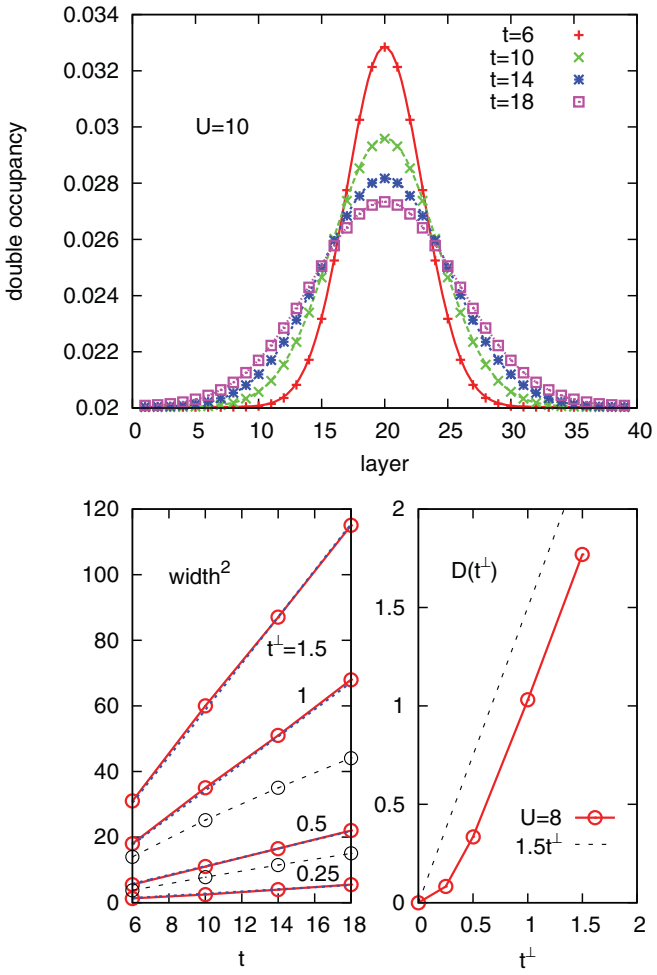

FIG. 4. (Color online) Top panel: Time-dependent distribution of the double occupancy in a 39-layer system with $U = 10$, after a pulse excitation with $\Omega \approx 12$ applied to the middle layer. Lines show a fit to a Gaussian centered at the middle layer. The bottom left panel plots the widths extracted from such fits as a function of time for different values of the interlayer hopping. The squared width grows linearly in $t - t_{\rm pulse}$, where $t_{\rm pulse} \approx 1.7$ is the time corresponding to the center of the pulse. Dashed lines show results with phonon bath (see text). The bottom right panel shows the dependence of the diffusion constant D on the interlayer hopping.

in the excitation density, the terms "double occupancy" and "number of doublons" differ by a constant only and will be used interchangeably.

As shown in the top panel of Fig. 4 (results for $U = 10$), already a short time after the pulse, the distribution of the photoexcited doublons (symbols) can be well fitted by a Gaussian (lines). (Note that there is an identical diffusion of holes, since the model is particle hole symmetric.) For interlayer hopping $t^\perp = 1$, the 39-layer system allows us to track the motion of the doublons up to $t \approx 20$. Extracting the widths of the Gaussians and plotting them as a function of time (Fig. 4, lower left panel), we find that the square of the width grows proportional to $t - t_{\rm pulse}$, indicating diffusive rather than ballistic motion. The doublon diffusion satisfies the expected law $d(m,t) - d_{\rm eq}(m,t) \sim \exp[-(m-20)^2/(4Dt)]$ ($m = 20$ is the central layer), with diffusion constant $D \approx 1.03t^\perp$ for $t^\perp = 1$. As long as the doublon-holon recombination is slow enough and the carriers are inserted with large kinetic energy, the diffusion of doublons and holes is not influenced much by the interaction strength. Within our numerical accuracy, we find the same diffusion constant for $U = 7$, 8, 9 and, 10, even though $U = 7$ is already close to the metal-insulator crossover.

On the other hand, a smaller interlayer hopping of course slows down the diffusion. The lower left panel of Fig. 4 plots the time evolution of the squared width of the distribution, for $t^\perp$ ranging from 0.25 to 1.5 ($U = 10$). (Because of the rapid spreading of the charge carriers we cannot study much larger values of $t^\perp$.) The diffusion constant $D(t^\perp)$, which is extracted from linear fits to these curves, grows roughly quadratically with $t^\perp$ for small $t^\perp$, while the dependence becomes almost linear for $t^\perp \gtrsim 0.5$ (Fig. 4, lower right panel).

In equilibrium, the diffusion constant is related to the conductivity $\sigma_{\rm dc}$ (with the charge e set to one) and the compressibility $\frac{\partial n}{\partial \mu}$ via the Einstein relation (or fluctuation-dissipation relation)

$$D\frac{\partial n}{\partial \mu} = \sigma_{\rm dc}. \tag{33}$$

Truly ballistic transport is thus expected for integrable one-dimensional systems (see Ref. 39 and references therein), which can have a perfect conductivity [i.e., a finite Drude weight $\sigma_{\rm dc} \sim \mathcal{D}\delta(\omega)$ for $\omega \to 0$] even at temperature $T > 0$.[40] For the Hubbard model in higher dimensions, the rather large width of the spectral function $A_{k\sigma}(\omega)$ in the Mott insulator indicates that the scattering time of a single particle excitation with momentum $\boldsymbol{k}$ is of the order of the inverse hopping, and hence its mean-free path is not much larger than a few lattice spacings. Only in a Fermi liquid at $T = 0$ would one expect infinite scattering times for electrons at the Fermi surface.

To some extent, the behavior of $D(t^\perp)$ shown in the lower right panel of Fig. 4 is qualitatively consistent with a quasiequilibrium argument based on the Einstein relation for large temperature T: Starting from the DMFT expression for the bulk conductivity,[9,41]

$$\sigma_{\alpha\alpha'}(\omega) \propto \sum_{k\sigma} v_k^\alpha v_k^{\alpha'} \int_{-\infty}^{\infty} d\omega' \times \frac{A_{k\sigma}(\omega')A_{k\sigma}(\omega+\omega')[f(\omega') - f(\omega+\omega')]}{\omega} \tag{34}$$

($\alpha = \perp, \parallel$), the dc conductivity in the transverse direction and in the limit of high temperature ($T \gg$ bandwidth) is given by

$$\sigma_{\rm dc}^\perp \propto \frac{1}{4T}\sum_{k\sigma}(v_k^\perp)^2 \int_{-\infty}^{\infty} d\omega\, A_{k\sigma}(\omega)^2, \tag{35}$$

where $v_k^\perp = t^\perp \sin(k^\perp)$ is the band velocity perpendicular to the layers. The integral scales like 1/bandwidth, and the bandwidth is proportional to $t^\parallel$ for $t^\parallel \gg t^\perp$ (almost independent layers), and proportional to $t^\perp$ for $t^\perp \gg t^\parallel$. Thus $\sigma_{\rm dc}^\perp \sim t^\perp$ for $t^\perp \gg t^\parallel$ and $\sigma_{\rm dc}^\perp \sim |t^\perp|^2/t^\parallel$ for $t^\parallel \gg t^\perp$. Because $\frac{\partial n}{\partial \mu} \sim n/4T$ for large T, the same behavior is found for the diffusion constant $D(t^\perp)$. Physically, the behavior for small $t^\perp$ is consistent with a rate equation picture, where the transfer of a doublon from one layer to the next is given by Fermi's golden

rule $\Gamma \sim |t^{\perp}|^2 \mathcal{N}$, with a matrix element $\propto t^{\perp}$, and a density of states $\mathcal{N} \sim 1/t^{\parallel}$ that scales with the inverse bandwidth.

Although the Einstein relation agrees with the observed behavior on a qualitative level, such a quasiequilibrium theory cannot describe the spreading of doublons in detail. First of all, the initial perturbation of the system is strong, and it is neither clear on what time scale a local equilibrium description is valid, nor how well it would apply to a distribution that varies considerably over only a few lattice spacings. Since doublons and holes might cool down (lower their kinetic energy) while they spread in the bulk, equilibration could actually lead to the formation of Fermi liquid quasiparticles and a corresponding reconstruction of the electronic density of states, a process for which the time scale is not known. Examples where nonequilibrium conditions have a strong influence on the spreading of particles have been studied recently, for a cloud of weakly interacting ultracold atoms in an optical lattice (both fermions and bosons).[42–44] For example, when the cloud expands into an empty lattice, it behaves diffusive in the dense core, but in the tails the density is too low to equilibrate, resulting in a ballistic expansion.[43,44]

More detailed insight into the way in which doublons and holes spread into the bulk can be obtained from the time- and layer-dependent distribution function

$$A_m^<(\omega,t) = \frac{1}{\pi}\mathrm{Im}\int_0^\infty ds\, e^{i\omega s}\, G_m^<(t+s,t), \qquad (36)$$

which reduces to the "photoemission spectrum" $A^<(\omega,t) = A(\omega)f(\omega)$ in equilibrium and in pump-probe experiments on quasisteady states,[45] and from the corresponding spectral function $A_m(\omega,t)$ (with $G^<$ replaced by $-G^R$). To study this quantity we switch to a smaller system, so that longer simulation times become possible and the integral in Eq. (36) does not strongly depend on the upper cutoff. In the upper panel of Fig. 5 we plot the distribution function for a 15-layer system with $U = 10$, which is excited with a pulse with $\Omega \approx 12$ on the surface layer $L = 1$. (A "repeated" boundary condition is applied at layer 15.) On a given layer L ($L = 8$ is plotted in the figure), the weight in the upper Hubbard band grows with time as more doublons arrive. At later times, the distribution is shifted to lower frequencies, indicating some kind of cooling of the particles as they move into the bulk. Still, the distribution is clearly nonthermal at all times, and its width remains comparable to the width of the Hubbard band. In such a highly excited system, one cannot expect the formation of quasiparticle states. Indeed, we only observe a slight broadening of the spectral function, rather than a formation of a quasiparticle band.

Although the weight in the distribution function $A_m^<(\omega,t)$ appears after an increasing time delay as one moves further away from the surface, we find that the distribution at the earliest times (i.e., right after it has achieved some measurable weight) has a similar shape on different layers (Fig. 5, lower panel). The distribution resembles the initial photodoped distribution on layer 1, although the spectral function of the bulk layers is quite different from that of the surface layer, especially during the application of the pulse. This might be related to a coherent tunneling of the fastest carriers.

A detailed understanding of the various propagation effects at early and later times can be important to interpret the

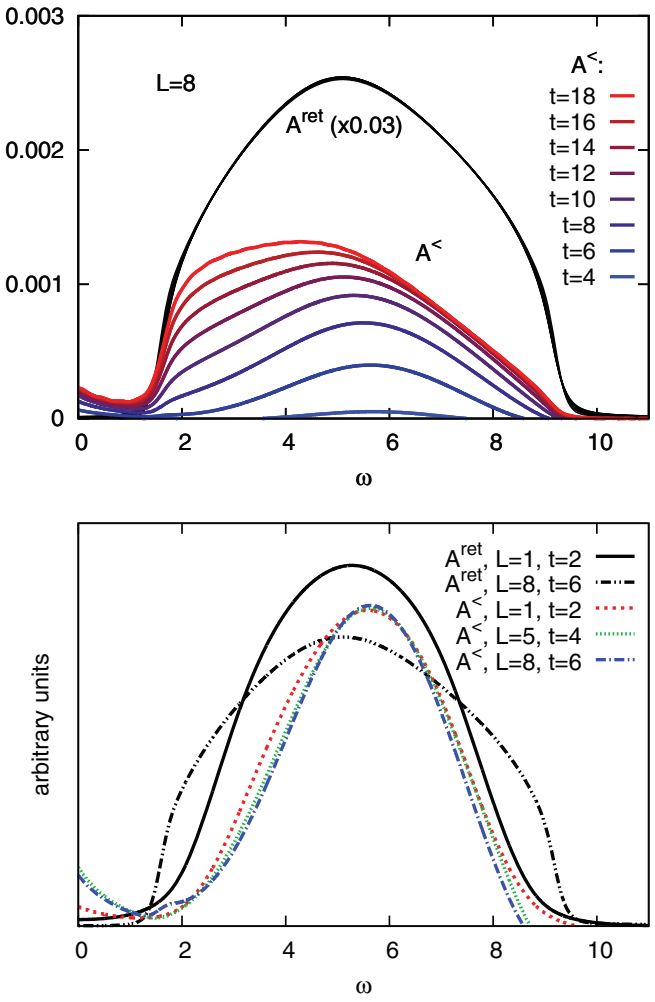

FIG. 5. (Color online) Spreading of doublons in a 15-layer system with $U = 10$ and pulse excitation with $\Omega \approx 12$ on layer 1. The top panel shows the increase of the occupied part of the spectrum in layer 8, and the relaxation of the carriers towards the bottom of the upper band. The bottom panel shows the spectral functions on layers 1 and 8 (solid and dashed black lines) and the occupied part of the spectrum in layers 1, 5, and 8 a short time after the injection of carriers (rescaled in such a way that the maxima are approximately the same). The distribution of the fastest carriers remains almost unchanged from layer 1 to 8.

relaxation of photoexcited carrier distributions in real experiments, since the dynamics is governed by both diffusion and local relaxation phenomena. In real materials, doublons and holes can dissipate their energy to other degrees of freedom as they diffuse into the bulk, e.g., to phonons or spin excitations, which are not correctly accounted for in the DMFT formalism for the isolated Hubbard model. To study the consequences of this dissipation, we have simulated the diffusion in the presence of a local phonon bath with $\omega_0 = 1$ and $\lambda = 1$. In this case the doublons and holes spread more slowly, as shown for $t^{\perp} = 1$ and $t^{\perp} = 0.5$ by the dashed lines in Fig. 4. A possible explanation is that the phonon cloud increases the effective mass of the carriers and hence reduces their diffusion coefficient. On the other hand, the curve for $t^{\perp} = 1.0$ also reveals a slight negative curvature, which indicates that the cooling

of the carriers influences the diffusion behavior in a nonlinear way.

C. Surface excitation of a heterostructure and doping by diffusion

An interesting application of the inhomogeneous DMFT is to study the dynamics in heterostructures. Experimentally, such artificially designed systems may provide a way to confine the excitation to a well-defined region of the sample (because, e.g., the pulse frequency can be tuned to the absorption band in certain layers), and induce controlled changes in the remaining layers. For illustration, we consider a heterostructure made of two different Mott insulators, and excite doublons and holes in the topmost layer. As illustrated in the top panel of Fig. 6, the system consists of five Mott insulating surface layers (red spectral functions) on top of a Mott insulating bulk, whose gap is much larger than the gap of the surface layers (blue spectral functions). The relative position of the Hubbard bands is chosen such that doublons can diffuse easily from the surface layers into the bulk, while the corresponding diffusion of holes into the bulk is prohibited.

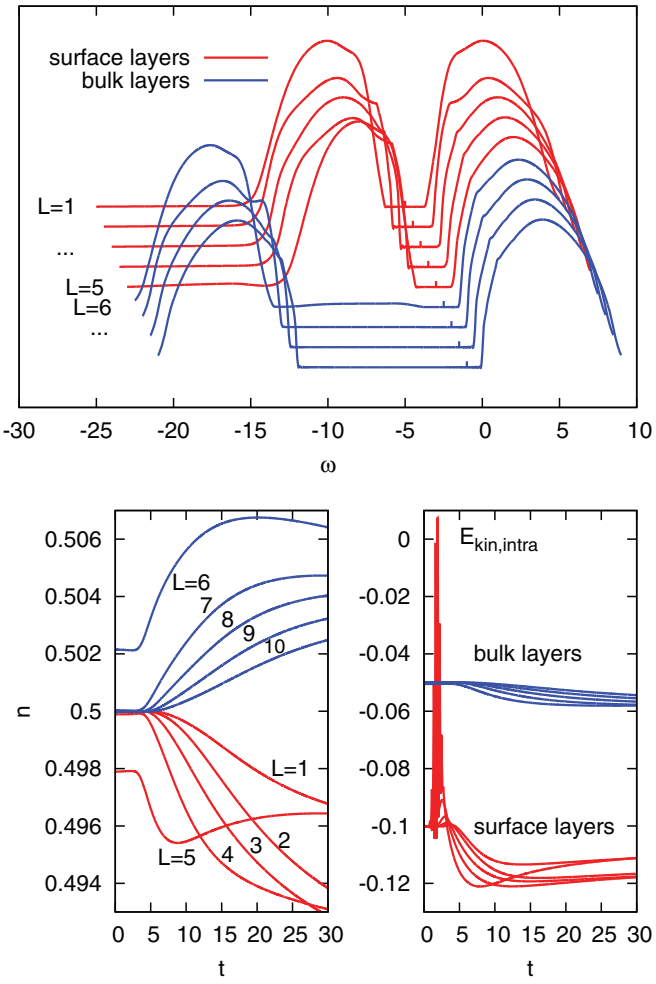

FIG. 6. (Color online) Top panel: Spectral functions for a heterostructure with five small-gap insulating layers (red, $U = 10$) on top of a bulk of large-gap insulator (blue, $U = 20$). The bands are shifted relative to each other in such a way that doublons can diffuse from the surface into the bulk, while holons cannot. The spectra are plotted with horizontal offsets of 0.3 and arbitrary vertical offsets. The tic marks indicate the position $\omega = 0$ within the Mott gap. Only four out of ten bulk layers are shown. Bottom panels: Time evolution of the filling and intralayer kinetic energy after excitation of the surface layer with a $\Omega \approx 12$ field pulse. (Phonon coupling $\lambda = 1$, phonon-frequency $\omega_0 = 1$, $\beta = 10$.)

The diffusion of charge carriers leads to a time-dependent doping of the neighboring layers with electrons and holes, and the special setup of Fig. 6 allows us to study the possible time-resolved emergence of a usual metallic state in the bulk layers, which are doped with electrons only. Explicitly, we simulated five surface layers with $U = 10$ on top of ten bulk layers with $U = 20$. We choose the vacuum boundary condition for the surface layer $L = 1$, and apply the in-plane electric field to this layer. To mimic dissipation to lattice and other degrees of freedom, which can accelerate the formation of a photodoped state with low kinetic energy and less scattering, we couple the system to local phonon baths, as described in the methods section and in Ref. 38. The phonon bath parameters are $\omega_0 = 1$ and $\lambda = 1$. (The small structures visible in the spectral functions near the gap edges are a result of this phonon coupling.)

The electron doping of the bulk and net hole doping of the surface layers can be seen in the bottom left panel of Fig. 6, which plots the time evolution of the density for the different layers. Note that even in the equilibrium system, a charge transfer occurs at the interface between surface and bulk layers, so that the first bulk layer is 0.2% electron doped, while the last surface layer is 0.2% hole doped. Figure 7 shows the time evolution of the double occupancy and the density on a color scale (gray scale). Initially the double occupancy is slightly larger in the surface layers, due to the smaller value of U. We find that the interface between the two insulating regions does not slow down the diffusion of doublons into the bulk layers, while holes stay confined to the surface layers. There is even an accumulation of doublons on the bulk side of this interface, which is explained by a small downward shift of the Hubbard band. The net charge in the surface layers is reduced as time increases due to the holes which diffuse back from the interface.

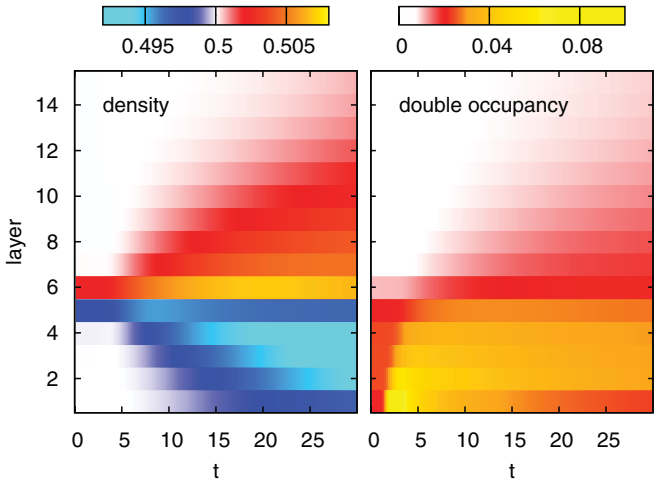

FIG. 7. (Color online) The left panel shows the time evolution of the density, and the right panel the time evolution of the double occupancy in the setup of Fig. 6.

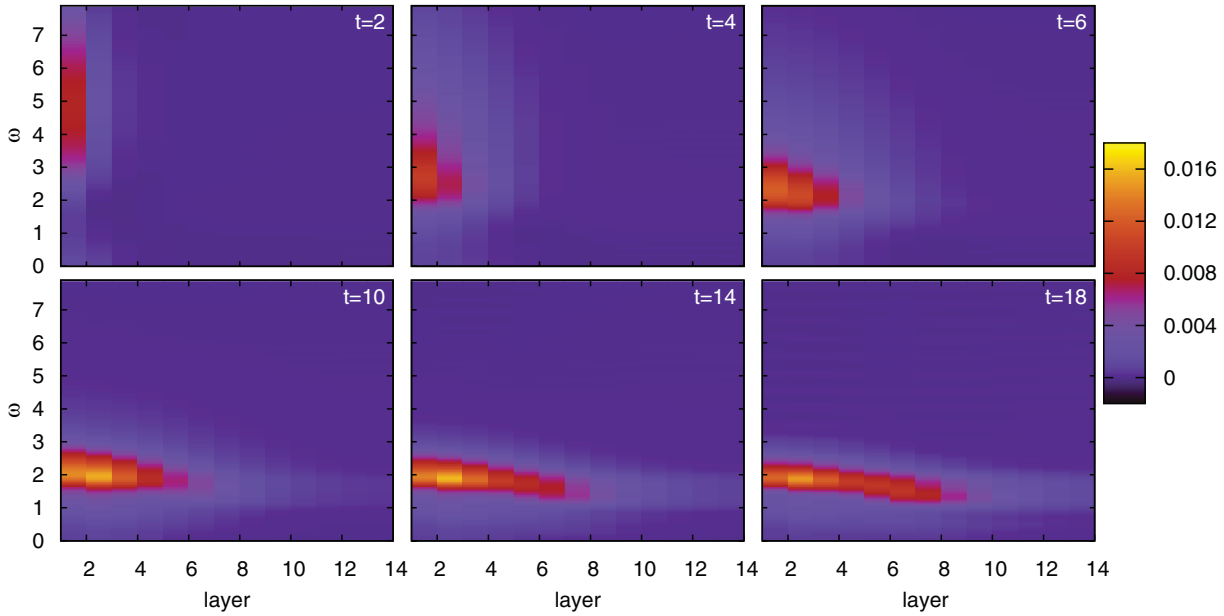

FIG. 8. (Color online) Occupation function $A^<(\omega,t)$ in the upper Hubbard band, for the same setup as Fig. 6. The excitation is an in-plane field pulse with frequency $\Omega \approx 12$ on the surface layer.

As a result of the dissipation, we expect the doublons and holes, which are created in the Hubbard bands of the $L = 1$ layer with a broad energy distribution, to cool down rapidly while they diffuse into the bulk. The latter effect should be evident as an accumulation of spectral weight in the distribution function (36) at the lower edge of the upper Hubbard band (and symmetrically for the holes). Figure 8 illustrates the time evolution of the occupied spectral function in the upper Hubbard band, which roughly covers the energy range $1.5 \lesssim \omega \lesssim 10$. The few-cycle pulse with $\Omega \approx 12$ creates doublons with a broad energy distribution centered at $\omega \approx 6$ (in the middle of the upper band). Such a broad spectrum is visible in the surface layer at $t = 2$ (the pulse lasts from about $t = 0.4$ to $t = 3$). Very quickly (second panel, $t = 4$) the doublons spread to the neighboring layers, and the cooling by the phonon bath leads to a shift of spectral weight to lower energies. Around $t = 6$, the diffusing doublons reach the bulk layers ($n \geqslant 6$). They keep diffusing into the bulk, which results in a net electron doping of the bulk layers. Furthermore, by $t = 10$, the phonon bath has removed most of the excess kinetic energy so that the changes in the spectral function at later times are mainly due to changes in the carrier density.

The decrease in the total in-plane kinetic energy in the different layers is also evident in the bottom right panel of Fig 6. This is consistent with a metallization of the bulk layers as a result of the doping induced by the diffusion of doublons. The small quantitative change of the kinetic energy is explained by the small amount of doping and the high effective temperature of the doped system. Despite the strong coupling to the phonon bath with inverse temperature $\beta = 10$, the distribution function $A^<(\omega,t)$ remains nonthermal within the accessible time range, and it is much broader than expected for the effective temperature of the bath. In addition, no pronounced quasiparticle peak emerges in the spectral function on these time scales. As in the case of a photodoped metallic state with electrons and holes,[38] it seems that the purely electron doped state obtained via doublon diffusion from the surface layer is not a good metal, and that the formation of a Fermi liquid state similar to an equilibrium chemically doped Mott insulator is a very slow process.

Finally, we note that in principle one should consider also the electrostatic energy associated with the (time-dependent) charge redistribution. This could be done for example by adding a layer-dependent Hartree potential $V_m(t)$ to the chemical potential in the DMFT loop. The formulas for this potential are given, for example, in Refs. 31, 34, 46, and 47:

$$V_m(\{n_1,\ldots,n_{m-1}\},t) = -\alpha \sum_{k=1}^{m-1} \sum_{l=1}^{k} [n_l(t) - n_{\text{background}}], \tag{37}$$

where $n_{\text{background}} = 0.5$ for half-filling and α is a constant proportional to the inverse dielectric constant. This potential would stop the spreading of charge into the bulk and confine the carriers to a region close to the interface. However, since the main purpose of the present work is to explain the nonequilibrium real-space DMFT method and to illustrate its versatility with several examples, we will leave the calculation of realistic time-dependent charge profiles in heterostructures to a future publication. (The results shown here are representative of materials with a large dielectric constant.)

D. Multilayer structures under applied bias

Transport through nanoscopic devices is another important area of physics that involves both nonequilibrium phenomena and strong correlations. The nonlinear current voltage characteristics of a two-terminal heterostructures has been studied previously, using an inhomogeneous steady-state DMFT approach.[48] The present formalism allows us to study the evolution of such systems in real time, and as a first application, we investigate the time-dependent build-up of

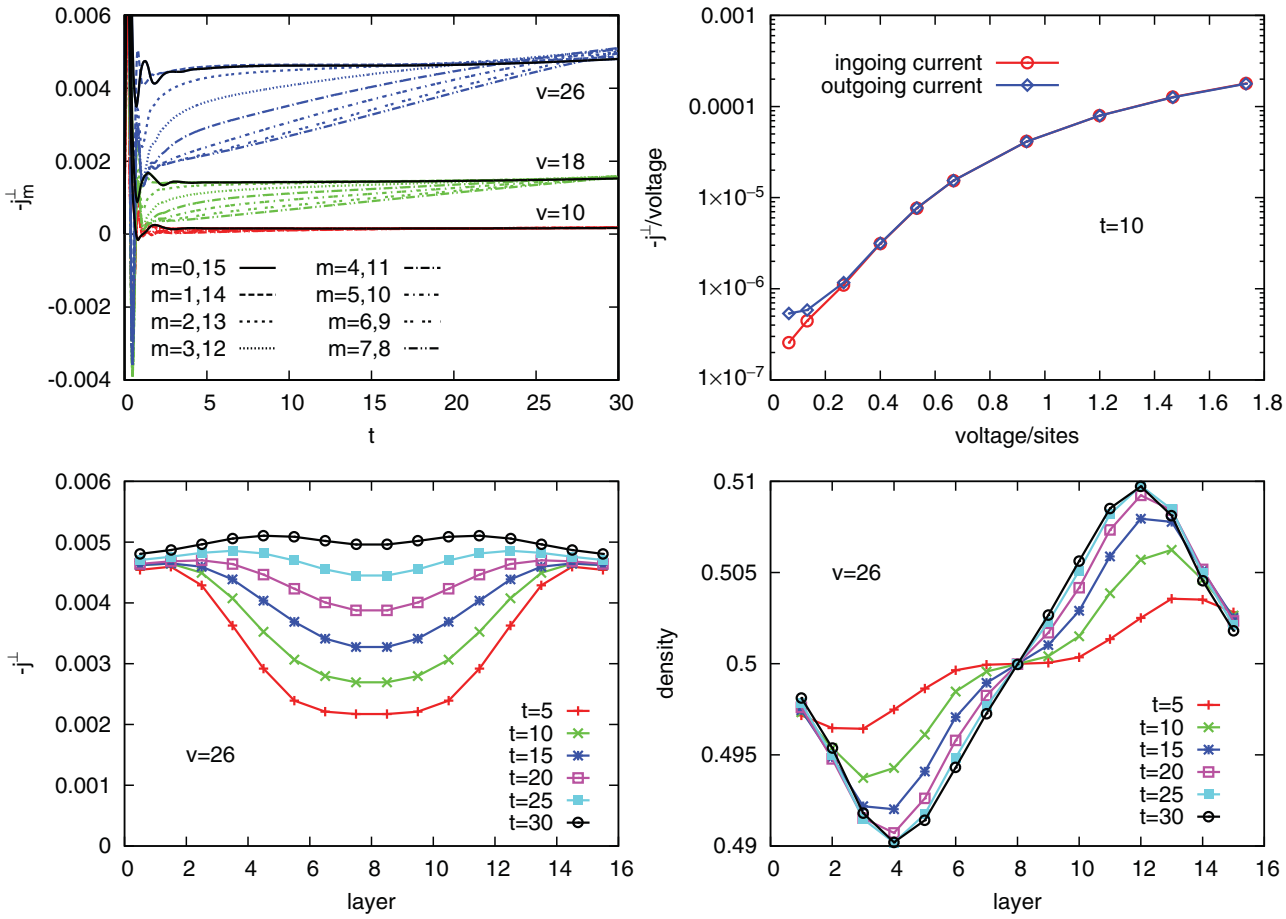

FIG. 9. (Color online) Top left panel: Current between the different layers of a 15-layer system with $U = 10$ as a function of time after the switch-on of a voltage bias v. The black line shows the current which flows into the system, which at the resolution of the plot is indistinguishable from the current which flows out. Top right panel: Current measured at the leads at $t = 10$, divided by voltage and plotted as a function of voltage, showing an exponential increase at low bias. The slope gives the threshold voltage for the dielectric breakdown of the Mott insulator. Bottom panels: Current and charge distribution at different times.

current and charge distributions across the sample after the switch-on of a voltage-bias perpendicular to the layers. We consider a system consisting of $L = 15$ correlated layers in the Mott regime ($U = 10$). In these calculations we do not attach local heat baths, so that energy dissipation occurs only in the leads, and may not be relevant on the time scales of our simulations. Initially, the system is in equilibrium without applied bias, and at time $t = 0$, we switch on a bias v across the whole sample, assuming that the voltage drop is linear, i.e., the electric field is $E^{\perp} = v/(N + 1)$. The top left panel of Fig. 9 shows the time evolution of the current $j^{\perp}$ flowing between the layers, for three different values of v. After some initial strong oscillations of the current $j^{\perp}$, which are related to the build-up of a polarization perpendicular to the layers, the currents into layer 1 ($j_0^{\perp}$) and out of layer 15 ($j_{15}^{\perp}$) quickly settle to some v-dependent value which changes only slowly with time (bold lines). This is in contrast to the currents between layers in the interior of the sample, which show a slower time evolution and no relaxation into a quasisteady state up to $t = 30$. The almost steady currents into and out of the leads exhibit a similar threshold behavior as was found in single-site DMFT calculations,[16,17] i.e., an exponential increase at low bias of the form $j^{\perp} \propto v \exp(-v_{\rm th}/v)$. This is illustrated in the top right panel of Fig. 9, which plots the in-going and out-going current at time $t = 10$ on a logarithmic scale.

In the bottom left panel of Fig. 9 we show current profiles within the structure at different times, for $v = 26$. At short times, the current is largest near the leads and smallest in the center. Around $t = 27$, the current deficit in the center changes into a current surplus (see also upper left panel), and we can expect some oscillations, until eventually an almost flat quasisteady state distribution is established. This current profile implies a redistribution of charge from the left side of the multilayer structure to the right side at short times. Indeed, a similar plot of the density distribution (bottom right panel) shows a build-up of positive (negative) charge in the left (right) half of the structure which progresses from the boundaries. At $t = 30$ the excess charge peaks at layers 4 and 12, which is in the middle of the left and right regions. The distribution in the quasisteady state might look similar. Again, one should in principle take the electrostatic potential associated with this charge redistribution into account and compute the potential profile across the structure self-consistently. However, if we insert the charge distribution at $t = 30$ into Eq. (37) we find that the voltage drop across the sample is modified by $\approx 0.3\alpha$, so that for α of $O(1)$ the induced Hartree potential is much

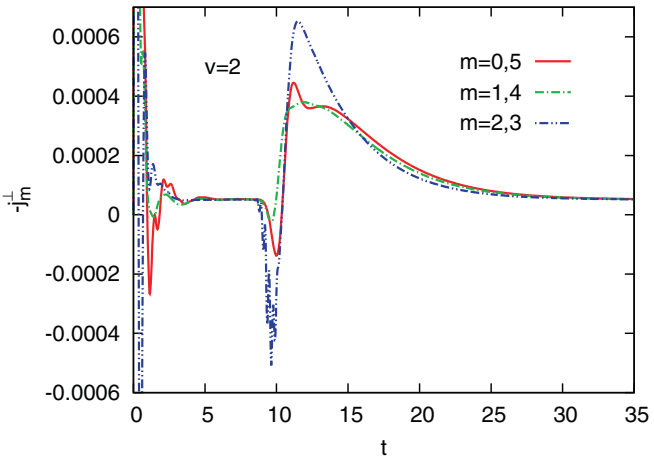

FIG. 10. (Color online) Current induced in a Mott insulating five-layer system ($U = 10$) under a voltage bias $v = 2$, by an in-plane field pulse acting on the middle layer. The pulse with $\Omega \approx 12$ is centered at $t_{\text{pulse}} = 9.3$. Initially the system is in equilibrium, and the large current spikes at short times are due to the build-up of a polarization after the switch-on of the linear bias.

smaller than the applied bias $v = 27$. In this case, we can expect that the self-consistent solution is very close to the result shown in the figure.

Similar time- and layer-dependent redistribution processes might be observable if they are triggered by a short pulse. To illustrate this, we finally discuss the current induced in Mott insulating structures under bias by an applied intralayer electric field pulse. We consider a five-layer structure with $U = 10$. The voltage $v = 2$ across the insulating sample is small enough that after the build-up of a polarization, there is only a very small current flowing through the sample (Fig. 10). Between $t = 8$ and $t = 11.6$ a field pulse with $\Omega \approx 12$ is applied to the middle layer (with polarization in the in-plane direction). At later times, the doublons and holes created by the pulse start to diffuse to the leads under the applied bias, which leads to a net negative current. The decay of this current is a direct measure for the mobilities. The intralayer current during the pulse exhibits a peak in the opposite direction to the expected bias-induced current in the central region, which indicates that the polarization in the central layers is reduced in response to the perturbation.

IV. CONCLUSIONS

We have described and tested the nonequilibrium extension of real-space DMFT, which allows us to study layered systems with strong electronic correlations. Like single-site DMFT (and in contrast to cluster extensions of DMFT), the formalism is based on the assumption of a purely local self-energy. One thus only has to solve a collection of (coupled) single-site impurity problems in a self-consistent manner. For a layer geometry, in which all properties of the system depend on only one space direction, the computational effort scales linearly with system size (up to the number of iterations, which may weakly depend on the system size), and the same is true for the storage requirement. We have discussed the details of our implementation based on self-consistent strong-coupling perturbation theory (NCA) as an impurity solver, but the formalism can equally be combined with a Monte Carlo,[49] or a perturbative weak-coupling solver.[13]

As an application, we have simulated the diffusion of photoexcited doublons in a Mott insulator, both inside the bulk, and from the surface of a heterostructure into the bulk. The diffusion constant was found to depend mainly on the intralayer hopping, while it is almost independent of the interaction strength. A heterostructure setup allows for a controlled doping of charge carriers of one type (e.g., doublons) into a Mott insulator, in contrast to photodoping, where always both electrons and holes are inserted. In principle, this opens the possibility to study the formation of quasiparticles in a metallic system. For the current setup, however, we find that the time scale for the build-up of such a state is rather long, such that the doped system behaves more like a bad metal on the numerically accessible time scales. A more thorough investigation of this important question will be deferred to a future study.

The second type of application was the layer- and time-resolved calculation of the current through a correlated insulating slab, where we reproduced the threshold behavior of the current-voltage characteristics known from previous nonequilibrium DMFT studies, and computed the evolution of the current and density profile after the switch-on of the voltage bias. We also considered a Mott insulating slab under bias (below the threshold for the dielectric breakdown) and computed the time-dependent redistribution of charge after a few-cycle laser pulse.

In the future, one should include the effect of the electrostatic potential to obtain a more realistic description of the diffusion of electrons and holes in a heterostructure. Also, the extension of our formalism to antiferromagnetically ordered layers would be useful, because this should allow us to exploit the cooling effect on the photodoped carriers associated with demagnetization.[21] How, and on which time scale, an almost thermal metallic state can be induced in a Mott insulator by diffusion of doublons from neighboring layers is an interesting topic for further studies.

ACKNOWLEDGMENTS

We thank H. Aoki, T. Oka, and N. Tsuji for helpful discussions. P.W. acknowledges support from FP7/ERC starting Grant No. 278023.

[1] M. Greiner, O. Mandel, T. W. Hänsch, and I. Bloch, Nature (London) **419**, 51 (2002).

[2] N. Strohmaier, D. Greif, R. Jördens, L. Tarruell, H. Moritz, T. Esslinger, R. Sensarma, D. Pekker, E. Altman, and E. Demler, Phys. Rev. Lett. **104**, 080401 (2010).

[3] H. Lignier, C. Sias, D. Ciampini, Y. Singh, A. Zenesini, O. Morsch, and E. Arimondo, Phys. Rev. Lett. **99**, 220403 (2007).

[4] J. Struck, C. Ölschläger, R. Le Targat, P. Soltan-Panahi, A. Eckardt, M. Lewenstein, P. Windpassinger, and K. Sengstock, Science **333**, 996 (2011).

[5]J. Simon, W. S. Bakr, R. Ma, M. E. Tai, Ph. M. Preiss, and M. Greiner, Nature (London) **472**, 307 (2011).
[6]A. L. Cavalieri, N. Müller, Th. Uphues, V. S. Yakovlev, A. Baltuska, B. Horvath, B. Schmidt, L. Blümel, R. Holzwarth, S. Hendel, M. Drescher, U. Kleineberg, P. M. Echenique, R. Kienberger, F. Krausz, and U. Heinzmann, Nature (London) **449**, 1029 (2007).
[7]S. Wall, D. Brida, S. R. Clark, H. P. Ehrke, D. Jaksch, A. Ardavan, S. Bonora, H. Uemura, Y. Takahashi, T. Hasegawa, H. Okamoto, G. Cerullo, and A. Cavalleri, Nat. Phys. **7**, 114 (2011).
[8]W. Metzner and D. Vollhardt, Phys. Rev. Lett. **62**, 324 (1989).
[9]A. Georges, G. Kotliar, W. Krauth, and M. J. Rozenberg, Rev. Mod. Phys. **68**, 13 (1996).
[10]P. Schmidt and H. Monien, arXiv:cond-mat/0202046.
[11]J. K. Freericks, V. M. Turkowski, and V. Zlatic, Phys. Rev. Lett. **97**, 266408 (2006).
[12]M. Eckstein, M. Kollar, and P. Werner, Phys. Rev. Lett. **103**, 056403 (2009).
[13]M. Eckstein, M. Kollar, and P. Werner, Phys. Rev. B **81**, 115131 (2010).
[14]M. Eckstein and Ph. Werner, Phys. Rev. Lett. **107**, 186406 (2011).
[15]A. Amaricci, C. Weber, M. Capone, and G. Kotliar, Phys. Rev. B **86**, 085110 (2012).
[16]M. Eckstein, T. Oka, and P. Werner, Phys. Rev. Lett. **105**, 146404 (2010).
[17]M. Eckstein and P. Werner, J. Phys.: Conf. Series **427**, 012005 (2013).
[18]C. Aron, G. Kotliar, and C. Weber, Phys. Rev. Lett. **108**, 086401 (2012).
[19]M. Eckstein and P. Werner, Phys. Rev. B **84**, 035122 (2011).
[20]N. Tsuji, T. Oka, P. Werner, and H. Aoki, Phys. Rev. Lett. **106**, 236401 (2011).
[21]P. Werner, N. Tsuji, and M. Eckstein, Phys. Rev. B **86**, 205101 (2012).
[22]N. Tsuji, M. Eckstein, and P. Werner, Phys. Rev. Lett. **110**, 136404 (2013).
[23]M. Potthoff and W. Nolting, Phys. Rev. B **59**, 2549 (1999).
[24]J. K. Freericks, Phys. Rev. B **70**, 195342 (2004).
[25]R. W. Helmes, T. A. Costi, and A. Rosch, Phys. Rev. Lett. **100**, 056403 (2008).
[26]E. V. Gorelik, I. Titvinidze, W. Hofstetter, M. Snoek, and N. Blümer, Phys. Rev. Lett. **105**, 065301 (2010).
[27]The names "real space DMFT" and "inhomogeneous DMFT" are both established in the literature, and we will use both terms interchangeably.
[28]R. W. Helmes, T. A. Costi, and A. Rosch, Phys. Rev. Lett. **101**, 066802 (2008).
[29]P. André, M. Schiró, and M. Fabrizio, Phys. Rev. B **85**, 205118 (2012).
[30]A. Ohtomo and H. Y. Hwang, Nature (London) **427**, 423 (2004).
[31]S. Okamoto and A. J. Millis, Nature (London) **428**, 630 (2004).
[32]H. Zenia, J. K. Freericks, H. R. Krishnamurthy, and Th. Pruschke, Phys. Rev. Lett. **103**, 116402 (2009).
[33]A. D. Caviglia *et al*., Phys. Rev. Lett. **108**, 136801 (2012).
[34]J. K. Freericks, *Transport in Multilayered Nanostructures: The Dynamical Mean-Field Theory Approach* (World Scientific, Singapore, 2006).
[35]M. Bonitz, *Progress in Nonequilibrium Green's Functions* (World Scientific, Singapore, 2000), and references therein.
[36]H. Keiter and J. C. Kimball, Int. J. Magn. **1**, 233 (1971); J. Appl. Phys. **42**, 1460 (1971).
[37]M. Eckstein and P. Werner, Phys. Rev. B **82**, 115115 (2010).
[38]M. Eckstein and P. Werner, Phys. Rev. Lett. **110**, 126401 (2013).
[39]J. Sirker, R. G. Pereira, and I. Affleck, Phys. Rev. Lett. **103**, 216602 (2009).
[40]X. Zotos, F. Naef, and P. Prelovsek, Phys. Rev. B **55**, 11029 (1997).
[41]Th. Pruschke, D. C. Cox, and M. Jarrell, Phys. Rev. B **47**, 3553 (1993).
[42]St. Mandt, A. Rapp, and A. Rosch, Phys. Rev. Lett. **106**, 250602 (2011).
[43]U. Schneider, L. Hackermüller, J. Ph. Ronzheimer, S. Will, S. Braun, Th. Best, I. Bloch, E. Demler, St. Mandt, D. Rasch, and A. Rosch, Nat. Phys. **8**, 213 (2012).
[44]J. Ph. Ronzheimer, M. Schreiber, S. Braun, S. S. Hodgman, S. Langer, I. P. McCulloch, F. Heidrich-Meisner, I. Bloch, and U. Schneider, Phys. Rev. Lett. **110**, 205301 (2013).
[45]J. K. Freericks, H. R. Krishnamurthy, and T. Pruschke, Phys. Rev. Lett. **102**, 136401 (2009); M. Eckstein and M. Kollar, Phys. Rev. B **78**, 245113 (2008).
[46]T. Oka and N. Nagaosa, Phys. Rev. Lett. **95**, 266403 (2005).
[47]M. Charlesbois, S. R. Hassan, R. Karan, D. Senechal, and A.-M. S. Tremblay, Phys. Rev. B **87**, 035137 (2013).
[48]S. Okamoto, Phys. Rev. Lett. **101**, 116807 (2008).
[49]P. Werner, T. Oka, and A. J. Millis, Phys. Rev. B **79**, 035320 (2009).